Title
Atomization off thin water films generated by high-frequency substrate wave vibrations

Journal
Physical Review E, 86(5)

ISSN
2470-0045

Authors
Collins, David J
Manor, Ofer
Winkler, Andreas
et al.

Publication Date
2012-11-01

DOI
10.1103/physreve.86.056312

Peer reviewed

Atomization off thin water films generated by high-frequency substrate wave vibrations

David J. Collins,[1,4] Ofer Manor,[2,4] Andreas Winkler,[3] Hagen Schmidt,[3] James R. Friend,[2,4] and Leslie Y. Yeo[2,*]

[1]*Monash University, Clayton, Victoria 3800, Australia*

[2]*Micro/Nanophysics Research Laboratory, RMIT University, Melbourne, Victoria 3000, Australia*

[3]*IFW Dresden, Dresden, Freistaat Sachsen D-01069, Germany*

[4]*The Melbourne Centre for Nanofabrication, Clayton, Victoria 3800, Australia**

(Received 10 September 2012; published 20 November 2012)

Generating aerosol droplets via the atomization of thin aqueous films with high frequency surface acoustic waves (SAWs) offers several advantages over existing nebulization methods, particularly for pulmonary drug delivery, offering droplet sizes in the 1–5-μm range ideal for effective pulmonary therapy. Nevertheless, the physics underlying SAW atomization is not well understood, especially in the context of thin liquid film formation and spreading and how this affects the aerosol production. Here, we demonstrate that the film geometry, governed primarily by the applied power and frequency of the SAW, indeed plays a crucial role in the atomization process and, in particular, the size of the atomized droplets. In contrast to the continuous spreading of low surface energy liquids atop similar platforms, high surface energy liquids such as water, in the present case, are found to undergo transient spreading due to the SAW to form a quasisteady film whose height is determined by self-selection of the energy minimum state associated with the acoustic resonance in the film and whose length arises from a competition between acoustic streaming and capillary effects. This is elucidated from a fundamental model for the thin film spreading behavior under SAW excitation, from which we show good agreement between the experimentally measured and theoretically predicted droplet dimension, both of which consistently indicate a linear relationship between the droplet diameter and the mechanical power coupled into the liquid by the SAW (the latter captured by an acoustic Weber number to the two thirds power, and the reciprocal of the SAW frequency).

DOI: 10.1103/PhysRevE.86.056312 PACS number(s): 47.35.Rs, 47.55.nd, 47.61.−k

I. INTRODUCTION

Surface acoustic waves (SAWs), beyond their versatile potential for rapid and controllable microfluidic actuation [1,2], have the powerful ability for easily atomizing liquids to generate micron dimension aerosol droplets [3–6]—a capability that is important in numerous processes from spray painting, inhalation therapy, and mass spectrometry to inkjet, agricultural, and more recently bioprinting. SAW atomization, in both standing [7] and traveling [8] wave configurations, has considerable advantages over other conventional nebulizers, and, in particular, ultrasonic atomization, in that it uses significantly less power, does not require orifices (e.g., nozzles) or meshes, is suited to producing aerosols within the size range of 1–5 μm for optimal inhalation therapy [9], and can be operated using a simple chip-scale platform comprising a piezoelectric substrate patterned with interdigital transducers (IDT) by means of standard photolithographic techniques [10] or coupled to a superstrate [11,12]. In addition, it has been shown that SAW atomization can be used to rapidly synthesize single and even multilayered composite polymer nanoparticles [13–15] or to rapidly produce polymer array patterns on substrates without necessitating physical or chemical templating [16]. Further, the typically high frequencies and low powers required for atomization do not result in shear- or cavitation-induced molecular damage, especially large biomolecules such as DNA, peptides, or proteins [17], which is particularly crucial for applications in pulmonary drug delivery [9,18] or mass spectrometry [19–21].

Despite the progress in demonstrating the potential of SAW atomization for these applications, there is a remarkable lack of physical and theoretical insight into the mechanisms underpinning atomization and, in particular, the relationship between the SAW frequency and power with the dimension of the resultant atomized droplets; the SAW frequency, in particular, has long been touted as a means for controlling the droplet size, crucial to any aerosolization process. Early attempts to study ultrasonic [22,23] and SAW [13,24] atomization simply proposed correlations between the aerosol dimension and the applied frequency. Subsequent work, in contrast, attempted to unravel the physics governing the atomization process by employing scaling theory to reveal the dominant role of capillary and viscous stresses in the destabilization of the air-liquid interface leading towards its breakup to form atomized droplets, and provided experimental measurements of the free surface vibration to dispel the prevailing view that the SAW frequency plays a dominant role in governing the atomized droplet dimension; instead, these studies hinted at the influence of the geometry of the source liquid (either a sessile drop or a thin film) spreading atop the atomization platform under SAW excitation, from which the atomized drops are ejected [5,25]. It was suggested that thin film geometries led to smaller droplets and higher atomization rates compared with that obtained using sessile drops as the source liquid geometry [5,17], although this was based on scaling arguments and preliminary experimental observations.

Here, we study the mechanism by which various system parameters (in particular, the applied frequency and power) govern the spreading of SAW-induced thin liquid films atop atomization platforms [17], and how the characteristics of the thin film, as a consequence, influence the size of the

*Corresponding author: leslie.yeo@rmit.edu.au

atomized droplets. Water films are assumed here, not merely for simplicity, but because water is a common drug excipient and carrier for biological agents in aerosol applications. In particular, we elucidate the specific mechanism controlling the thickness of the spreading film, highlighting the behavior of these high surface energy water films in distinct contrast to the behavior of low surface energy silicone oil films [26]: the discrepancy between the continuous spreading of silicone oil films and the transient spreading of water films leading to their quasisteady behavior is directly related to the characteristic difference observed in the resultant film heights.

The rest of the paper is organized as follows. In Sec. II, we briefly discuss the current physical understanding of the mechanics underpinning SAW atomization. This is followed by a description of the experimental procedure carried out to investigate SAW atomization in Sec. III. We then formulate a theory to model the spreading of the water film in Sec. IV, from which we obtain predictions for the quasisteady film shape. These predictions then facilitate a comparison with the experimental data in Sec. V. Finally, we summarize our findings in Sec. VI.

II. SAW ATOMIZATION

Unlike *bulk* ultrasonic transducers, the SAW energy is isolated along the *surface* of the piezoelectric substrate that constitutes the atomization platform, exponentially decaying within a few wavelengths into the substrate depth. When the SAW comes into contact with the leading edge of the liquid, however, it is diffracted into the liquid phase at the *Rayleigh angle* $\theta_R = \sin(c_l/c_s)$ subtended to the vertical axis, where c_l is the sound velocity in the liquid and c_s is the SAW velocity on the substrate [2,27]. The SAW thus comprises an efficient energy transfer mechanism from the solid substrate to the liquid, and generates sound waves in the liquid that give rise to an acoustic radiation pressure [28] as well as a streaming flow that is a consequence of a collection of mechanisms [1], including Eckart streaming [29,30] and Schlichting streaming [31,32]. The acoustic radiation pressure is a consequence of the steady, time-averaged stress imparted on the drop-film interface due to the mismatch in the acoustic impedance across the interface upon the impact and subsequent reflection of the sound waves. Eckart flow is a steady vortical flow in the liquid bulk arising from the energy dissipated during viscous attenuation of axially polarized sound waves over length scales much larger than the sound wavelength in the liquid, whereas Schlichting streaming describes flow within a submicron-thick viscous boundary layer immediately adjacent to the substrate surface along which the SAW traverses [32]. Despite its confinement, the latter is, nevertheless, not only capable of altering the contact angle between the liquid body and solid substrate, but also displacing the three-phase contact line [33,34]. As such, the acoustic radiation pressure and both the Eckart and Schlichting streaming mechanisms are likely to govern the geometry and wetting properties of the parent liquid on the atomizing platform.

The influence of these properties on the atomization process, in particular, and hence on the size and production rate of the aerosol droplets has been previously implied [5]. Atomization ensues above a threshold power [5,35] beyond which capillary forces are no longer able to stabilize the interface from perturbations imposed by the substrate acceleration and the consequent streaming in the parent liquid. The dimension of the ejected droplets D, formed during the pinch-off and breakup of the destabilized wave crests, then corresponds to the most dangerous wavelength associated with the instability, which can be estimated from a dominant capillary-viscous stress balance [5]

$$D \sim \lambda \sim \frac{\gamma H^2}{\mu f L^2}. \tag{1}$$

γ is the gas-liquid surface tension, μ the liquid shear viscosity, and f the SAW frequency, whereas H and L are the characteristic height and length scales of the parent liquid film or drop, respectively. We shall show later that the shape of the parent liquid film or drop (i.e., H and L) is dependent on the SAW frequency and amplitude. Of particular note in Eq. (1) is the $D \sim 1/f$ relationship, distinct from the $1/f^{2/3}$ scaling in correlations based on the subharmonic capillary wave excitation that have previously been reported, originally for ultrasonic transducers [22], but often prescribed wholesale for SAW atomization with little regard for the markedly different physics between the systems [24]. It is also questionable whether the small amplitude perturbation assumption implicit in the derivation of these linearized models holds, especially when the breakup of the interface to produce aerosol droplets during the atomization process is typically associated with large amplitude interfacial deformation. Below, we provide empirical evidence to support this inverse frequency scaling, *as yet unverified*. In addition, we note the influence of the aspect ratio H/L (i.e., the geometry of the parent liquid drop or film) on the ejected droplet size in Eq. (1): $H/L \sim 1$ for a sessile drop whereas $H \ll L$ for a thin film. We show that H is related to the wavelength of the sound waves generated in the liquid due to the leaky SAW, and develop a numerical simulation for the spreading of the quasisteady film to predict L as a function of the various system parameters; in particular, L is found to evolve with the mechanical power emitted by the SAW that is then transferred to the liquid. These H and L values are then used in Eq. (1) to predict the droplet sizes, which compares favorably with the trends observed in the experimental data acquired over the range of applied frequencies tested (13–124 MHz).

III. EXPERIMENT

We employed 13–132 MHz Rayleigh SAW devices comprising 7-nm chrome/175-nm gold interdigital transducers (IDTs) patterned using standard photolithography on a 0.5-mm thick 128° Y-cut, X-propagating single crystal lithium niobate (LN) piezoelectric substrate [10], as depicted in Fig. 1. We examined the following frequencies: 13.2, 18.9, 22.0, 26.4, 33.0, 44.0, 66.1, 99.1, 123.9, and 132.1 MHz using IDTs with 25, 33, 33, 33, 31, 29, 25, 20, 50, and 20 finger pairs, respectively. The SAW was generated by applying a sinusoidal electric voltage to the IDT using a signal generator (SML01; Rohde & Schwarz, North Ryde, NSW, Australia) and amplifier (10W1000C; Amplifier Research, Souderton, PA). The voltage across the SAW device, measured using an oscilloscope (Wavejet 332/334; LeCroy, Chestnut Ridge,

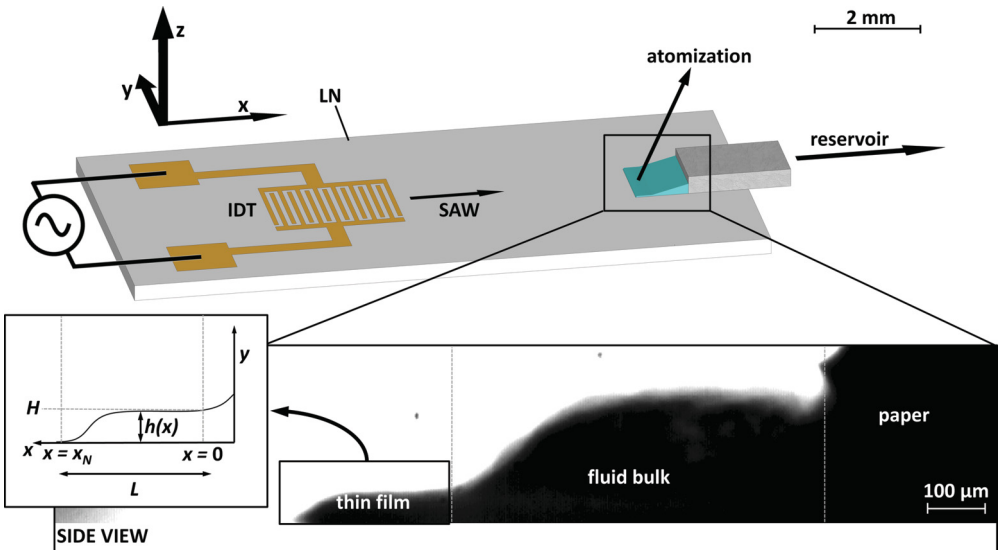

FIG. 1. (Color online) Schematic illustration of the SAW atomization device comprising a lithium niobate (LN) substrate on which interdigital transducer (IDT) electrodes were patterned. The liquid to be atomized was supplied from a reservoir (not shown) through a paper wick. As illustrated by the expanded-view image, the SAW drew out a meniscus from the paper, comprising a thin advancing film and a bulk region, both of which are characterized by different length scales, capillary frequencies, and resultant droplet sizes. The majority of the atomized droplets, however, originated from the thin film region with characteristic height and length scales denoted by H and L, respectively, both of which are small compared to the width of the film, which, in turn, is set by the width of the paper wick.

NY), then determines the SAW surface-normal displacement velocity, subsequently measured using a laser Doppler vibrometer (LDV, UHF–120; Polytec GmBH, Waldbronn, Germany); this was also used to verify the existence of a traveling SAW. Under SAW excitation, the liquid to be atomized (deionized water; Milli-Q 18.2 MΩ.cm, Millipore, Billerica, MA), initially housed in an external reservoir, was delivered to the SAW device for atomization using a capillary wick consisting of polyester-cellulose clean room paper (C1; LymTech, Chicopee, MA) with a width similar to that of the IDT aperture, and that was placed in contact with the edge of the device [17], as illustrated in Fig. 1. The SAW device itself was placed on a Peltier cooler (CP85438; CUI Inc., Tualatin, OR) to mitigate spurious effects from evaporation, a step not previously taken in other SAW atomization experiments. The film spreading dynamics were observed using a high-speed camera (iSpeed, Olympus, Yokohama, Japan) at 1500–10 000 fps, whereas droplet sizes were measured via laser diffraction (Spraytec, Malvern Instruments, Malvern, UK); three separate measurements over a 15 s duration were taken for each SAW frequency.

Contact between the edge of the wetted paper wick and the hydrophilic LN substrate surface led to the formation of a meniscus between the two substrates, as sketched in Fig. 2(a). Under the influence of SAW beyond a sufficient power level, the meniscus was observed to spread in a direction opposite to that of the SAW propagation, forming a liquid bulk with characteristic height and length scales that are several times the sound wavelength in water λ_l [Fig. 2(b)]. The pullout of water from the wetted paper is known to result from the interaction between the flow in a thin viscous boundary layer that forms in the meniscus immediately above the LN substrate and the free air-water interface [26,32,34]. Further spreading of the water body atop the LN substrate then results in two characteristic fluctuating regions [Fig. 2(c)]: a bulk region adjacent to the paper that retains a similar characteristic length and thickness as before, and a thin front-running film region with a characteristic length roughly corresponding to two SAW wavelengths (i.e., $L \equiv 2\lambda_{\mathrm{SAW}}$) and a thickness that appears to scale with λ_l. Next, we discuss the mechanism and parameters that govern the characteristic height H and length L of this thin front-running film region, whose interface subsequently breaks up to produce the atomized droplets [Fig. 2(d)].

IV. THEORY

A. Film height

We treat the interaction between the SAW-induced sound wave in the liquid, emitted from the LN surface ($y = 0$) at an angle $\theta_R \approx 22^\circ$ to the vertical y axis (see Fig. 1), and the free air-water interface ($y = h$) as a simplified model in which the sound wave is emitted from a simple piston, offset from the horizontal axis $y = 0$ by θ_R towards a horizontal fully reflecting surface at $y = h$. To leading order in θ_R, the piston can be assumed horizontal ($y = 0$), emitting sound waves along the vertical y axis with a wavelength equal to the vertical component of the original sound wavelength $\lambda_v = \lambda_l \cos\theta_R$. Under these conditions, the time-averaged energy density in the liquid between the piston and the free surface of the film follows [28]

$$\langle E \rangle \approx \frac{\rho \xi_0^2 \omega^2 (\beta + 1)}{4\beta \cos^2(2\pi h/\lambda_v) \sin^2(2\pi h/\lambda_v)}, \tag{2}$$

where ρ, ξ_0 and $\omega = 2\pi f$ are the liquid density, SAW vertical displacement amplitude, and SAW angular frequency, respectively, as seen in Fig. 3(a). The heights $h/\lambda_v = n/4$ ($n = 1,2,3,\ldots$) correspond to acoustic resonance modes with

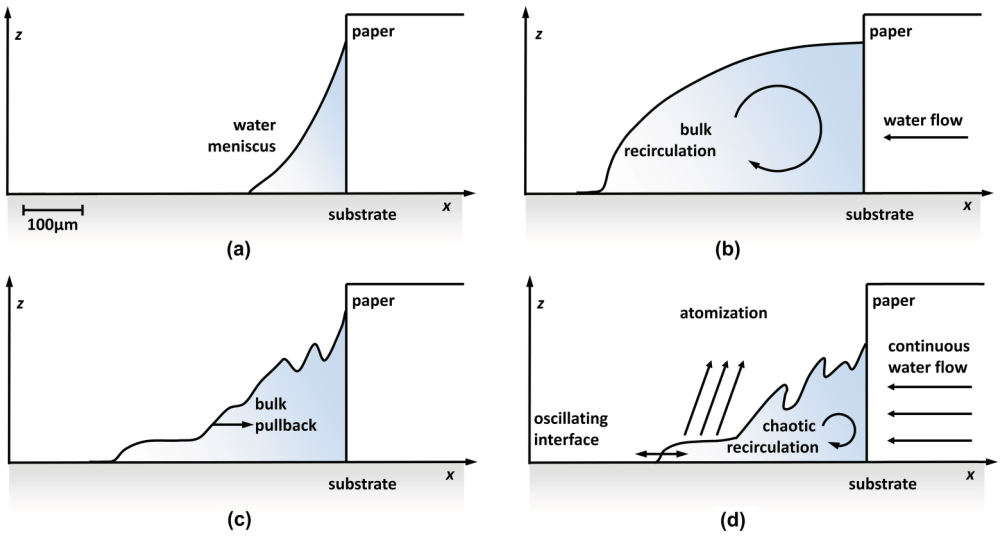

FIG. 2. (Color online) (a) At rest and prior to SAW actuation, a liquid meniscus formed between the wetted paper and the LN substrate. (b) Application of the SAW results in the pullout of a liquid bulk with height and length scales several times the liquid wavelength λ_l. (c) After ~50–500 ms, the leading edge of the liquid bulk was observed to retreat, (d) leaving behind a thin film region from which atomization occurred. The film and chaotic bulk liquid regions interacted dynamically, with the film moving horizontally and occasionally being obscured completely by the bulk region.

an unbounded acoustic energy density in the film, delivering an unbounded radiation pressure intensity at and normal to the planar liquid free surface and rendering an inevitable change in the film inclination or thickness until the acoustic resonance is suppressed. On the other hand, $h/\lambda_v = n/8\,(n = 1,3,5,\ldots)$ is associated with the local minima in the acoustic energy density, a balance between this in the form of the corresponding local minima in radiation pressure intensity with the capillary stress then leads to stable film heights. Depending on the initial height of the film, or the height of the region from which the thin film is pulled out [for example, the bulk region to the right of $h\,(x = 0)$ in the inset of Fig. 1], the film then assumes an equilibrium height at the next energy minima [Fig. 3(b)]. In this case, the thin advancing film at the far left of Fig. 3(c) is observed to obey $h \approx 7/8\lambda_v$ at different applied frequencies and power levels. In fact, we observe, quite uniquely for thin liquid films, the entire film and bulk region in its transient state to occasionally exhibit traits of such energy minimization, apparent in the stable *stair-stepping* of the film height at multiple odd integers of one-eighth wavelengths seen in Fig. 3(c). In an earlier study [26], silicone oil films drawn out from a similar platform by SAWs were observed to follow $h \approx 3/8\lambda_v$ [see the lone experimental point denoted by the square in Fig. 3(b)]. The reason for the difference in the characteristic film height between water and silicone oil is as yet unclear, although the key difference between water and silicone oil is in the surface tension, roughly 72 mN/m for water and 20–30 mN/m for silicone oil, which renders a different initial three phase contact angle formed between each liquid and the solid substrate (roughly 10–20° for silicon oil and 60–70° for water at rest). In any case, having found a relationship that estimates the characteristic film height $H \approx 7/8\lambda_v$ to be used subsequently in Eq. (1), we now turn to formulate a model that describes the mechanism governing the film length l.

B. Film length

The thin film geometry in the inset of Fig. 1 is governed by an interplay between capillary and acoustic effects; the latter is excited by SAWs that propagate at the substrate surface in the direction opposite to that of the film spreading [26], and comprise compressional motion in the liquid film that, to first approximation, can be modeled as the horizontal and vertical particle displacement of a sound wave in an unbounded fluid [36]

$$s_x = \xi_0 e^{j\omega t} e^{-jk_L x} e^{-\alpha k_L z},$$
$$s_z = -j\alpha\xi_0 e^{j\omega t} e^{-jk_L x} e^{-\alpha k_L z}, \tag{3}$$

respectively. Here, the attenuation of the sound wave is neglected since the characteristic sound attenuation length scale $4\rho c_l^3/3\omega^2\mu \approx 0.1$–$0.01$ m [37] is large compared to the thickness of the thin film for the range of frequencies investigated. In the above, x and z are the horizontal and vertical coordinates in the film, respectively, originating at the liquid-solid interface and the neck bordering the thin film and the water bulk shown in Fig. 1, t is time, and, $k_L = k_r + jk_i$ is the SAW wave number, taken to be a constant with the complex component $k_i^{-1} \approx \rho_s c_s \lambda_{SAW}/\rho c_l \approx 9\lambda_{SAW}$ representing the SAW characteristic attenuation length under an unbounded fluid [38] and $\alpha = [1 - (c_s/c_l)^2]^{-1/2}$; ρ_s is the substrate density. The nonisotropic Rayleigh acoustic radiation pressure on the free surface of the film may then be described by [34]

$$\mathbf{p_r} = \left\langle \frac{\mathbf{vv}}{2\,|\mathbf{v}|^2} + \mathbf{I}\frac{B}{4A} \right\rangle \rho\,|\mathbf{v}|^2\,, \tag{4}$$

where $|\mathbf{v}| = |\partial \mathbf{s}_x/\partial t, \partial \mathbf{s}_z/\partial t| \approx \xi_0\omega$ is the magnitude of the harmonic sound particle velocity, $\mathbf{I}$ is the identity tensor, and A and B are Fox and Wallace coefficients [39], respectively; the angled parentheses denote the time averaging of the inner quantity [i.e., $\langle\zeta\rangle \equiv (1/2\pi)\int_0^{2\pi} \zeta\, dt$].

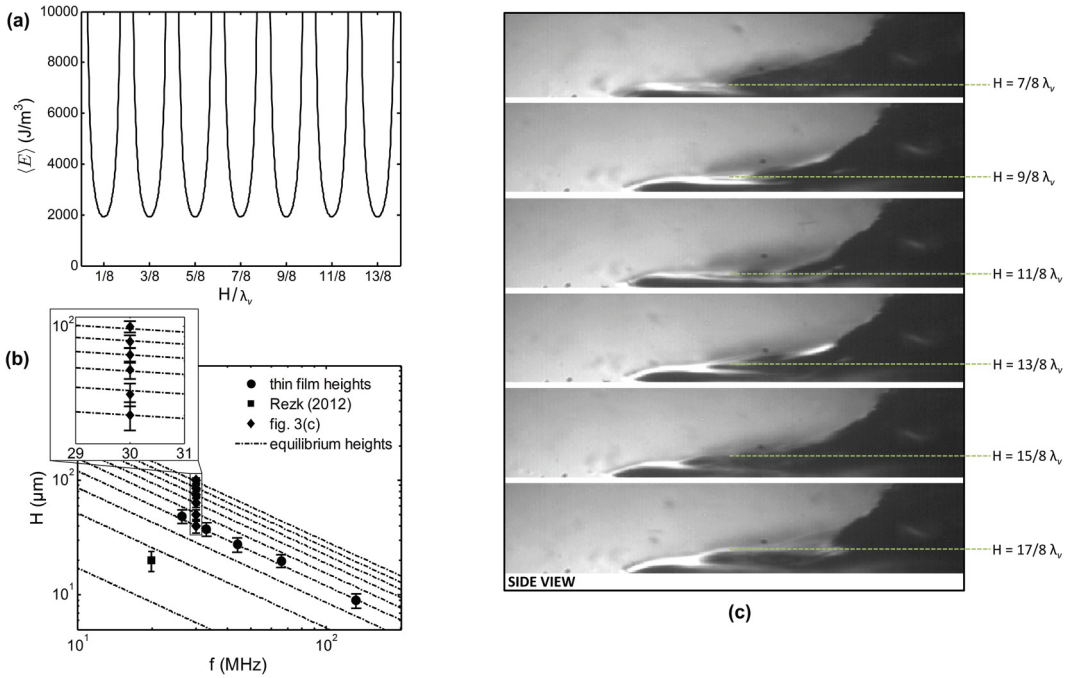

FIG. 3. (Color online) (a) Acoustic energy density, wherein local energy minima occur at odd one-eight integers of the vertical component of the sound wavelength $\lambda_v = \lambda_l \cos\theta_R$, calculated here for $\omega/2\pi = 33$ MHz and $\xi_0 = 7.3$ nm. This corresponds to an acoustic Weber number $\mathrm{We} \equiv \rho(\xi_0\omega)^2 L/\epsilon\gamma$, a measure of the power applied to the film, of 7.7; $\xi_0\omega$ is the characteristic velocity of the elements in the fluid as the sound wave traverses and L is twice the SAW wavelength. (b) The circle data points represent equilibrium film heights H (Fig. 1) and are observed to correspond to the local energy minima, or more specifically, seven-eighths times the vertical component of the wavelength $\lambda_v = \cos(\theta_R)\lambda_l$. The SAW frequencies associated with the experimental points from left to right are 26.5, 33.0, 44.0, 66.1, and 132.1 MHz, and the corresponding range in We numbers, which do not appear to significantly contribute to the thin film height, are (4.2–13.1), (3.7–14.8), (5.5–9.1), (2.4–6.8), and (1.1–2.4), respectively. The square data point at 20 MHz is taken from an earlier study [26] where silicone oil in place of water was used and the diamond data points (magnified in the figure inset) represent the equilibrium and additional transient film heights between $7/8\lambda_v$ and $17/8\lambda_v$, observed with a 30 MHz device. (c) Upon initial application of the SAW, a transient state can develop in which the water meniscus exhibits different stable heights that correspond to odd one-eighth multiple integers in addition to the $7/8\lambda_v$ equilibrium height. This image was taken of a liquid meniscus in the same setup as that described in Fig. 1 when subject to a 30 MHz signal, modulated here with a 300 Hz sinusoidal amplitude signal to prolong the transient stage of the thin film formation, thus enabling us to capture it.

Over short $\mathcal{O}(\omega^{-1})$ time scales, mass and momentum transfer are governed by Eq. (3). Over long times, mass and momentum transfer commensurate with the hydrodynamic time scales are governed by the second-order steady component of the flow field, generated by the $\mathcal{O}(|\mathbf{v}|)$ SAW and the corresponding sound particle velocity in Eq. (3). After expanding the continuity and Navier-Stokes equations in a small parameter defined by the Mach number $\mathrm{Ma} = |\mathbf{v}|/c_l$ and subsequent time averaging, these satisfy [29,40]

$$\nabla \cdot \mathbf{u} = 0, \tag{5}$$

$$-\nabla p + \mu\nabla^2\mathbf{u} + \mathbf{F} = 0, \tag{6}$$

to $\mathcal{O}(v_0\mathrm{Ma})$. Here, $\mathbf{u}$ and p are the steady components of the second-order velocity and hydrodynamic pressure fields in the film and $\mathbf{F} = -\langle\rho(\mathbf{v}\cdot\nabla)\mathbf{v} + \mathbf{v}(\nabla\cdot\rho\mathbf{v})\rangle$ is an effective body force over long times that originates from the divergence of the Reynolds stress tensor $\rho\mathbf{vv}$. The appropriate boundary conditions are then prescribed by the no-slip condition at the solid substrate

$$\mathbf{u}|_{z=0} = 0, \tag{7}$$

the normal stress jump at the free surface $z = h$

$$-(p\mathbf{I} + \mathbf{p_r})\cdot\mathbf{n} + \mu(\nabla\mathbf{u} + \nabla\mathbf{u}^T)\cdot\mathbf{n} = \gamma\nabla\cdot\mathbf{nn}, \tag{8}$$

where $\mathbf{n}$ is the outer unit normal to the air-water interface, and mass conservation in the film

$$\frac{\partial h}{\partial t} = -\frac{\partial(\overline{u}_x h)}{\partial x}. \tag{9}$$

We now expand the equations and boundary conditions that govern the nonvanishing (over long times) flow component [i.e., Eqs. (5)–(8)] in the small parameter $\epsilon \equiv H/L$ and ignore the next order correction in Ma, justified by the difference in magnitudes between $\epsilon \approx 10^{-1}$ and $\mathrm{Ma} \approx 10^{-3}$; given that H and L are small compared to the width of the film, which, in turn, is determined by the width of the paper wick, it is not unreasonable to assume a two-dimensional model. The problem is then rendered dimensionless using the following set of transformations:

$$\left(x, k_L^{-1}\right) \to \left(x, k_L^{-1}\right) L, \quad (z,h) \to (z,h)\, H, p \to (\epsilon\gamma/L)\, p,$$
$$(u_x, u_z) \to \left(\epsilon^3\gamma/\mu\right)(u_x, \epsilon u_z), \tag{10}$$

in which the scaling for the velocity and force in the film are chosen to satisfy the balance between acoustic streaming and

capillary effects. Omitting $O(\epsilon)$ and smaller contributions, the integral mass and momentum conservation equations in the quasisteady film are then given by [41]

$$\frac{\partial}{\partial x}\int_0^h u_x\, dy = 0, \tag{11}$$

$$\frac{\partial^2 u_x}{\partial z^2} = \frac{\partial p}{\partial x} - F_x. \tag{12}$$

Due to the small attenuation of the SAW and thus the sound wave in Eq. (3) (i.e., $k_i \ll 1$) the horizontal component of the body force when in contact with the thin film may be expressed as [36]

$$F_x = -\mathrm{We}\left(1+\alpha_1^2\right)k_i, \tag{13}$$

where $\mathrm{We} \equiv \rho(\xi_0\omega)^2 L/\epsilon\gamma$ is an *acoustic* Weber number that captures the relative contributions from the inertial forcing and the stabilizing capillary stresses. In addition, the absence of any externally applied pressure gradients

$$\frac{\partial p}{\partial z} = 0, \tag{14}$$

together with Eq. (8) then renders the scaled hydrodynamic pressure

$$p \approx -\frac{\partial^2 h}{\partial x^2}. \tag{15}$$

Finally, the boundary conditions on the solid substrate and at the free surface are

$$u_x|_{z=0} = 0, \qquad \frac{\partial u_x}{\partial z}|_{z=h} = 0. \tag{16}$$

Equations (8), (11), (12), and (16) then give rise to the quasisteady thin film equation

$$\frac{\partial}{\partial x}\left[h^3\left(\frac{\partial p}{\partial x} - F_x\right)\right] = 0, \tag{17}$$

where, owing to the weak attenuation of the SAW along the thin front-running film region (see Fig. 1), the contribution of the radiation pressure p_r to the hydrodynamic pressure p, mediated by Eq. (14), is roughly uniform, therefore eliminating any net contribution of p_r to the film shape in Eq. (17). The boundary conditions at the interface in the neck between the thin film and bulk regions (Fig. 1) can then be specified by

$$h|_{x=0} = 1, \qquad \left.\frac{dh}{dx}\right|_{x=0} = 0. \tag{18}$$

Given the highly smooth, chemically homogeneous, and hydrophilic nature of the LN substrate, and following [34], we postulate that the three-phase contact angle at the advancing front of the thin film at $x = x_N$ vanishes under the high applied powers required for SAW atomization. The mechanism responsible for the vanishing contact angle arises from the interaction between the dominant Schlichting flow [32] and the free surface in a viscous boundary layer immediately above the substrate possessing a characteristic thickness $\delta \equiv (\mu/\rho\omega)^{1/2}$, where the contributions from the bulk flow considered earlier are small. It can then be assumed that the vanishing contact angle gives rise to the existence of a thin front-running precursor film with a thickness that scales as δ, irrespective of the bulk flow, such that the following boundary conditions can be imposed:

$$h|_{x\to\infty} \approx \delta/H, \qquad \left.\frac{dh}{dx}\right|_{x\to\infty} = 0. \tag{19}$$

Equations (17) to (19) were solved numerically using the MATLAB boundary value problem solver bvp4c [42]. Rather than using a coordinate transformation to handle the infinite domain, the computational spatial domain was limited to a maximum length of 20 units to reasonable accuracy, allowing for a numerical error below 0.1% on a mesh of 10 000 points. The calculated geometry was further found to be insensitive to arbitrary values of the precursor film thickness, spanning $[0.1\delta/H, 10\delta/H]$.

V. RESULTS AND DISCUSSION

Equation (17) presents the competing mechanisms that govern the thin film geometry, whereby the capillary pressure within the film, mediated by the hydrodynamic pressure p, minimizes the deformation of the free surface; in the absence of SAW, the acoustic stresses embodied by the volume force F_x are absent and the meniscus then spreads to form a film that completely covers the solid substrate under the fully wetting condition of Eq. (18). Under the influence of external acoustic stresses, however, the body force F_x drives an opposing flux of liquid volume in the SAW propagation direction from the thin film *back* towards the water reservoir. Ignoring rapid fluctuations that occur on the free surface of the film, this competition between the capillary and acoustic volume force then leads to a quasisteady film shape over long times that satisfies global volume conservation (i.e., no net volume flux across the film cross section). Figure 4 shows the effect of We on the quasisteady film shape: increasing We, equivalent to higher applied powers and hence surface displacement velocities, leads to an increase in the acoustic body force F_x, that, in turn, generates a larger volume flux from the film towards the reservoir, resulting in a shorter film length. The numerical solution decays with an increase in We and appears to agree well with experimental measurements of the maximum length of the thin film region observed, defined as the distance from the end of the bulk region [i.e., $x = 0$ (taken to be at the intersection between the height of the uniform thin film region $y = H$ with the tangent of the curved free surface just outside the film in the bulk region)], to the location of the apparent contact line at $x = x_N$, as sketched in the inset of Fig. 1; $x = x_N$ is determined at the limit of visual detection where the film height corresponds to one pixel in the experimental digital image.

To further quantify the decay in the film length with We, we introduce the functional form of the normal stress at the free surface and acoustic body force in the film, and omit the noncontributing radiation pressure term. The Weber number We may then be eliminated from the film equation [Eq. (17)] by rescaling the spatial coordinate as $x \to xL\mathrm{We}^{-1/3}$ in place of the preceding scaling to give the generalized film equation

$$\frac{\partial}{\partial x}\left\{h^3\left[\frac{\partial^3 h}{\partial x^3} - \left(1+\alpha_1^2\right)k_i\right]\right\} = 0. \tag{20}$$

Equation (20) underscores the balance between the competing capillary and acoustic body forces, rendering the film length

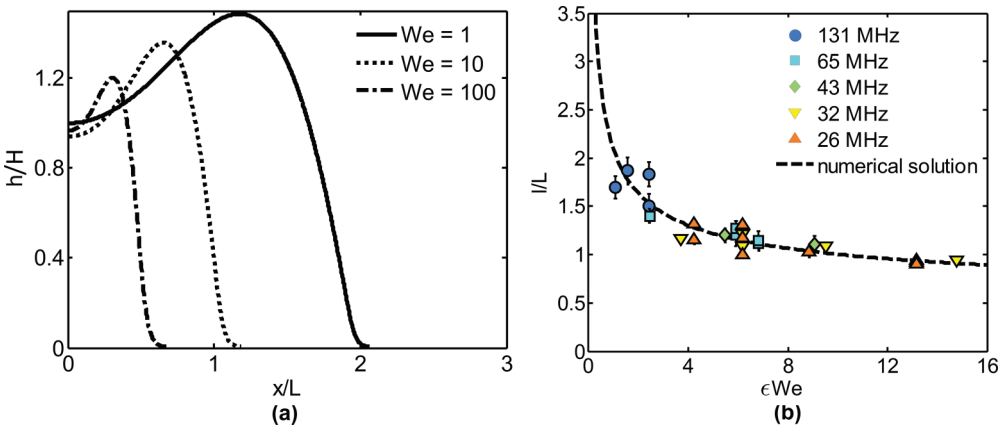

FIG. 4. (Color online) (a) Quasisteady film shape for different acoustic Weber numbers $\mathrm{We} = \rho(\xi_0\omega)^2 L/\epsilon\gamma$. Higher powers (and hence surface displacement velocities) and larger SAW wavelengths are observed to give rise to shorter films. (b) Single measurements of scaled maximum observed film lengths l/L for different applied frequencies (26–131 MHz) and powers (2.6–10.2 W), with resulting We values showing good agreement with the numerical result predicted by the solution of Eq. (17). It can be seen that both the experimentally measured and numerically predicted film lengths progress to an asymptote beyond $\epsilon\mathrm{We} \gtrsim 4$. The error bars indicate the measurement error related to the pixelation of the original digital imagery.

to decay as $\mathrm{We}^{-1/3}$ and generalizing the result shown in Fig. 4(b).

Although a thin film was clearly observed, the *onset* of atomization only occurred above a critical $\epsilon\mathrm{We} \approx 1$. Above $\epsilon\mathrm{We} \gtrsim 4$, however, we observe the film length l to be insensitive to We. Given that H is fixed for a given applied frequency (Sec. IV A), it then follows from Eq. (1) that the ejected droplet dimension scales with the inverse of the applied frequency, which was first suggested in [5] but without experimental corroboration. This $1/f$ relationship for the droplet dimension, distinct from the $1/f^{2/3}$ scaling previously suggested [22–24], is therefore experimentally verified for the first time here in Fig. 5(b) in which the droplet sizes are the mass median diameters obtained from the size distribution of the ejected droplets [an example of which is shown in Fig. 5(a) for an applied frequency of 22 MHz]. The trimodal distribution in Fig. 5(a) is typical of that observed across the range of frequencies employed: The small and intermediate droplet sizes, with peaks close to mass median diameters of approximately 1 (peak 1) and 15 μm (peak 2), originated from droplets that were observed to be ejected from the thin film region (Fig. 1), whereas the largest droplets corresponding to the last peak at the extreme right with dimensions on the order of 100 μm were observed to be ejected from the bulk region (Fig. 1). These large droplets can be excluded from the following discussion as the model in the current study pertains solely to the dynamics of the thin film region.

In particular, we recall from Sec. IV A that the film height, in dimensional terms, can be approximated by $h \sim H \approx 7/8\lambda_v$, implying that $h \sim H \sim 1/f$. Since $L \equiv 2\lambda_{\mathrm{SAW}} \sim 1/f$ and thus $l \sim L\mathrm{We}^{-1/3} \sim \mathrm{We}^{-1/3}/f$, it then follows that both h and l scale inversely with f, and consequently the film aspect ratio $h/l \sim H/\left(L\mathrm{We}^{-1/3}\right)$ is independent of f and is instead dependent on We, or, more specifically, the mechanical power transmitted by the SAW into the liquid, manifested by the term $\rho\xi_0^2\omega^2$ in the definition of We. Correcting for the actual film aspect ratio h/l in place of the characteristic power independent height to length scale ratio H/L in Eq. (1) then leads to

$$D \sim \frac{\gamma H^2}{\mu L^2}\frac{\mathrm{We}^{2/3}}{f}, \tag{21}$$

suggesting that the ejected droplet sizes scale linearly with $\mathrm{We}^{2/3} f^{-1}$, consistent with that observed in Fig. 5(b).

VI. CONCLUSION

SAW atomization comprises a powerful means for the generation of micron dimension aerosol droplets from a miniature microfluidic platform for various applications across spray painting, mass spectrometry, and drug delivery. The key advantages of the platform are its low power, miniaturizability into a small handheld portable platform, and, due to the high frequencies employed, the absence of shear or cavitation damage to biomolecules—an important criterion if the device is to be used for pulmonary delivery of next generation therapeutics such as peptides, proteins, and nucleic acids. Nevertheless, little is understood about the physics associated with SAW atomization systems; in the absence of work to revisit the fundamentals, there has been a tendency to inappropriately adopt theories developed for bulk ultrasonic atomization, rather inappropriate due to the substantial differences in the nature and mechanics of the acoustic excitation between the two methods of atomization.

Here, we examined the mechanisms that underpin the hydrodynamics associated with SAW atomization of droplets from a thin liquid film source, with the intent of providing a more rigorous verification of the role of the parent liquid source geometry and hence the inverse frequency scaling of the atomized droplet dimension alluded to in a previous study [5]. The size of water droplets produced from the atomization of a spreading meniscus drawn out by the SAW from a wet permeable paper strip connected to a reservoir was measured using laser diffraction. These appear to have different sizes depending on the region along the elongated meniscus film they are atomized from. Larger 100 μm droplets

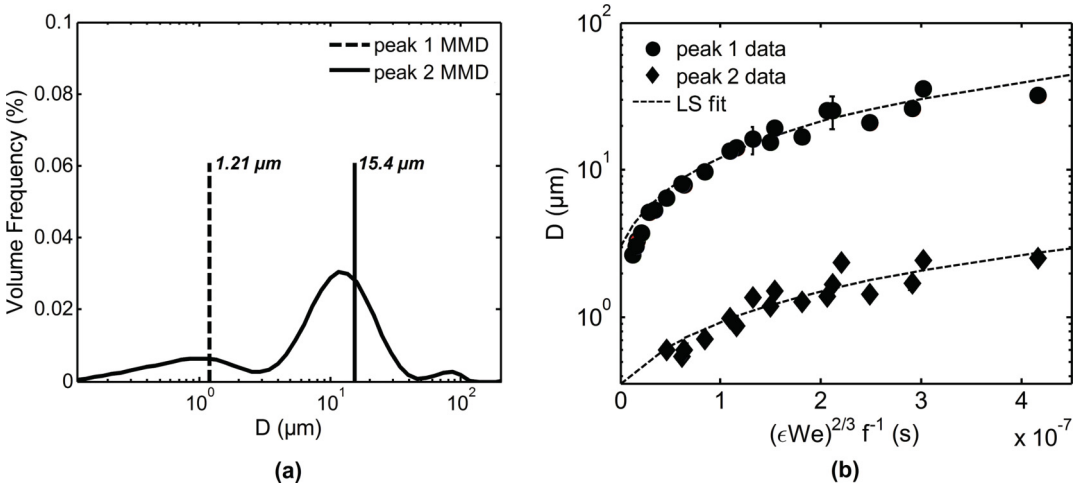

FIG. 5. (a) Experimentally measured aerosol size distribution via laser diffraction, obtained at $\omega/2\pi = 22$ MHz and an applied power of 5.2 W, corresponding to $\epsilon\mathrm{We} = 8.0$; these data are also a qualitative representation of the results obtained at other applied frequencies and powers. Three distinct peaks in the droplet sizes are observed. Peaks 1 and 2 correspond to droplets produced as a consequence of atomization off the thin film region illustrated in Fig. 1 with mass median diameters (MMDs) D of 1.21 and 15.4 μm and standard deviations of 1.04 and 9.4, respectively, computed from the volume frequency histogram of discrete droplet diameters. A third peak comprising droplets with diameters on the order of 100 μm can also be seen. These droplets are ejected from the bulk region illustrated in Fig. 1 (as only very few droplets are ejected from this region, these are not the subject of the present study that focuses on atomization from the thin film region). (b) Variation in the mass median droplet diameter D with $(\epsilon\mathrm{We})^{2/3} f^{-1}$. The data points represent the experimentally measured droplet MMD data for a range of frequencies (13–124 MHz) for each of the two peaks (i.e., peak 1 and peak 2) with droplets produced via atomization from the thin film region, and the dotted lines represent least-squares (LS) linear fitting, demonstrating the linear relationship between D and $(\epsilon\mathrm{We})^{2/3} f^{-1}$. Error bars show one standard deviation between the three 15 s measurements taken at each frequency. We also note that peak 1 failed to develop at lower values of $(\epsilon\mathrm{We})^{2/3} f^{-1}$, where frequencies exceed 98MHz ($\epsilon\mathrm{We} \lesssim 1$).

were ejected from a bulk liquid region immediately adjacent to the edge of the paper strip from which the meniscus is drawn. Smaller droplets, of typically submicron and micron dimension that are relevant for inhalation therapy, however, were ejected from a thin front-running film ahead of the bulk region. Given the interest in the use of SAW atomization to obtain large quantities of these small aerosol droplets, we focused our investigation on the spreading dynamics of this thin film region, for which a theoretical model was derived. A numerical simulation to predict the equilibrium shape of the thin film as a function of relevant system parameters revealed that the length of the thin film region was determined from a competition between capillary and acoustic forces, captured through a dimensionless acoustic Weber number, that over long times balances to form a quasisteady film. Good agreement was obtained between the theoretically predicted and experimentally measured film lengths for a range of applied powers (2.6–10.2 W) and frequencies (26–131 MHz). The film height, on the other hand, is determined by self-selection of the energy minimum state associated with the acoustic resonance present in the liquid film. Not only do we verify the resultant inverse frequency scaling using the height and length predictions with the experimental measurements, we also, for the first time, explicate the role of the applied power beyond simply influencing the onset of atomization at a critical SAW amplitude: Increasing the power drives stronger streaming in the film in the direction opposite to its spreading, therefore producing shorter films, that, in turn, lead to larger droplets, at least at moderate power levels. The film length, nevertheless, was observed to approach an asymptotic limit at higher powers, diminishing its influence on the droplet sizes as the power is further increased.

[1] J. Friend and L. Yeo, Rev. Mod. Phys. **83**, 647 (2011).
[2] L. Y. Yeo and J. R. Friend, Biomicrofluidics **3**, 012002 (2009).
[3] K. Chono, N. Shimizu, Y. Matsui, J. Kondoh, and S. Shiokawa, Jpn. J. Appl. Phys. **43**, 2987 (2004).
[4] M. Kurosawa, T. Watanabe, A. Futami, and T. Higuchi, Sens. Actuators A: Physical **50**, 69 (1995).
[5] A. Qi, L. Yeo, and J. Friend, Phys. Fluids **20**, 074103 (2008).
[6] J. Ju, Y. Yamagata, H. Ohmori, and T. Higuchi, Sens. Actuators A: Physical **145**, 437 (2008).
[7] J. Ju, Y. Yamagata, H. Ohmori, and T. Higuchi, Sens. Actuators A: Physical **147**, 570 (2008).
[8] M. Alvarez, J. Friend, and L. Yeo, Nanotechnology **19**, 455103 (2008).
[9] A. Qi, J. Friend, L. Yeo, D. Morton, M. McIntosh, and L. Spiccia, Lab Chip **9**, 2184 (2009).
[10] R. White and F. Voltmer, Appl. Phys. Lett. **7**, 314 (1965).
[11] R. P. Hodgson, M. Tan, L. Yeo, and J. Friend, Appl. Phys. Lett. **94**, 024102 (2009).

[12] J. Reboud, R. Wilson, Y. Zhang, M. H. Ismail, Y. Bourquin, and J. M. Cooper, Lab Chip **12**, 1268 (2012).
[13] J. Friend, L. Yeo, D. Arifin, and A. Mechler, Nanotechnology **19**, 145301 (2008).
[14] M. Alvarez, L. Y. Yeo, J. R. Friend, and M. Jamriska, Biomicrofluidics **3**, 014102 (2009).
[15] A. Qi, P. Chan, J. Ho, A. Rajapaksa, J. Friend, and L. Yeo, ACS Nano **5**, 9583 (2012).
[16] M. Alvarez, J. Friend, and L. Yeo, Langmuir **24**, 10629 (2008).
[17] A. Qi, Y. Yeo, J. Friend, and J. Ho, Lab Chip **10**, 470 (2009).
[18] L. Yeo, J. Friend, M. McIntosh, E. Meeusen, and D. Morton, Expert Opin. Drug Deliv. **7**, 663 (2010).
[19] S. Heron, R. Wilson, S. Shaffer, D. Goodlett, and J. Cooper, Anal. Chem. **82**, 3985 (2010).
[20] J. Ho, M. K. Tan, D. B. Go, L. Y. Yeo, J. R. Friend, and H.-C. Chang, Anal. Chem. **83**, 3260 (2011).
[21] S. H. Yoon, Y. Huang, J. S. Edgar, Y. S. Ting, S. R. Heron, Y. Kao, Y. Li, C. D. Masselon, R. K. Ernst, and D.-R. Goodlett, Anal. Chem. **84**, 6530 (2012).
[22] R. Lang, J. Acoust. Soc. Am. **34**, 6 (1962).
[23] F. Barreras, H. Amaveda, and A. Lozano, Exp. Fluids **33**, 405 (2002).
[24] M. Kurosawa, A. Futami, and T. Higuchi, in *Proceedings of the International Conference on Solid-State Sensors and Actuators* (Chicago, IL, 1997), pp. 801–804.
[25] M. Tan, J. Friend, O. Matar, and L. Yeo, Phys. Fluids **22**, 112112 (2010).
[26] A. R. Rezk, O. Manor, J. R. Friend, and L. Y. Yeo, Nat. Commun. **3**, 1167 (2012).
[27] K. Länge, B. Rapp, and M. Rapp, Anal. Bioanal. Chem. **391**, 1509 (2008).
[28] B. Chu and R. Apfel, J. Acoust. Soc. Am. **72**, 1673 (1982).
[29] C. Eckart, Phys. Rev. **73**, 68 (1948).
[30] J. Vanneste and O. Bühler, Proc. R. Soc. London A **467**, 1779 (2011).
[31] H. Schlichting, Phys. Z. **33**, 327 (1932).
[32] O. Manor, L. Y. Yeo, and J. R. Friend, J. Fluid Mech. **707**, 482 (2012).
[33] P. Brunet, M. Baudoin, O. B. Matar, and F. Zoueshtiagh, Phys. Rev. E **81**, 036315 (2010).
[34] O. Manor, M. Dentry, J. Friend, and L. Yeo, Soft Matter **7**, 7976 (2011).
[35] A. Yule and Y. Al-Suleimani, Proc. R. Soc. London A **456**, 1069 (2000).
[36] S. Shiokawa, Y. Matsui, and T. Ueda, in *Proceedings of the IEEE Ultrasonics Symposium* (IEEE, Tahoe, NV, 1989), pp. 643–646.
[37] J. Lighthill, J. Sound Vib. **61**, 391 (1978).
[38] R. Arzt, E. Salzmann, and K. Dransfeld, Appl. Phys. Lett. **10**, 165 (1967).
[39] F. Fox and W. Wallace, J. Acoust. Soc. Am. **26**, 147 (1954).
[40] W. Nyborg, J. Acoust. Soc. Am. **25**, 68 (1953).
[41] R. V. Craster and O. K. Matar, Rev. Mod. Phys. **81**, 1131 (2009).
[42] J. Kierzenka and L. Shampine, ACM Trans. Math. Software **27**, 299 (2001).